

# Heat alleviation studies on hypersonic re-entry vehicles

M. Khalid

[mkholid@kau.edu.sa](mailto:mkholid@kau.edu.sa)

K. A. Juhany

Department of Aeronautical Engineering

King Abdul Aziz University

Jeddah

Saudi Arabia

## ABSTRACT

A numerical simulation has been carried out to investigate the effects of leading edge blowing upon heat alleviation on the surface of hypersonic vehicles. The initial phase of this work deals with the ability of the present CFD-based techniques to solve hypersonic flow field past blunt-nosed vehicles at hypersonic speeds. Towards this end, the authors selected three re-entry vehicles with published flow field data against which the present computed results could be measured. With increasing confidence on the numerical simulation techniques to accurately resolve the hypersonic flow, the boundary condition at the solid blunt surface was then equipped with the ability to blow the flow out of the solid boundary at a rate of at least 0.01–0.1 times the free stream ( $\rho_\infty u_\infty$ ) mass flow rate. The numerical iterative procedure was then progressed until the flow at the surface matched this new ‘inviscid like’ boundary condition. The actual matching of the flow field at the ejection control surface was achieved by iterating the flow on the adjacent cells until the flow conformed to the conditions prescribed at the control surface. The conditions at the surface could be submitted as a  $\rho_\infty u_\infty$  at the surface or could be equipped as a simple static pressure condition providing the desired flow rate. The comparison between the present engineering approach and the experimental data presented in this study demonstrate its ability to solve complex problems in hypersonic.

**Keywords:** Hypersonic flow; heat transfer studies; computational fluid dynamics; re-entry vehicles; fluid injection; strong shock effects

## NOMENCLATURE

$\alpha$	angle-of-attack
$\delta_{ij}$	Kronecker delta
$a_n$	curve fit constants for the $c_p$ equation
$e$	internal energy
$q$	dynamic pressure, $1/2\rho V^2$
$C_i$	mass fraction
$C_p$	pressure coefficient, $(p - p_\infty)/q_\infty$
$c_p$	specific heat at constant pressure
$c_v$	specific heat at constant volume
$D_i$	molecular diffusion constant
$he$	static enthalpy
$h$	Plank's constant
$h_d$	dissociation enthalpy per unit mass of air in the external flow
$h_i$	dissociation energy per unit mass
$k$	Boltzmann's constant
$k_{th}$	thermal conductivity constant
$L$	model reference length
$L_e$	Lewis number
$\rho$	fluid density
$P$	pressure
$R$	gas constant
$R_B$	base radius
$R_N$	nose radius
$S$	distance from nose
$T$	temperature
$x_i$	co-ordinates ( $x_1 = x$ , $x_2 = y$ , $x_3 = z$ )
$u_i$	velocity vector
$V$	velocity magnitude
$E$	total energy per unit volume
$\tau_{ij}$	viscous stress tensor
$\varepsilon$	emissivity constant ( $\approx 1$ )
$\sigma$	Boltzmann constant
$\mu$	dynamic viscosity
$q$	heat flux
$q_{ref}$	heat flux at the stagnation point using Fay–Riddell method
$R_e$	Reynolds number
$Pr$	Prandtl number
$M$	Mach number
$( )_i$	mass injection boundary conditions
$( )_e$	edge of the boundary layer
$( )_\infty$	freestream conditions
$( )_{out}$	boundary outflow conditions
$( )_t$	turbulent quantity
$( )_w$	wall conditions
$( )_{oe}$	stagnation condition at the edge of the boundary layer

## 1.0 INTRODUCTION

Treating the hypersonic flow emerging from the strong shock immediately upstream of the blunt nose to reduce the heat flux to the re-entry vehicles is certainly not new. Other than increasing the nose bluntness radius itself, various protective techniques have been utilised with success, which include the use of high heat capacity materials on the surface with an ability to radiate much of the heat from the vehicle body. Hankey<sup>(1)</sup> and Stumpf<sup>(2)</sup> have given a detailed description of such methods. Application of such metals as Beryllium oxide or carbon-carbon composites and other carbon fibre and silicon-carbide (C-SC) or even tetra and borosilicate tiles as used on the shuttle, on the exposed surface can be made to efficiently radiate the heat away based on the Stephan-Boltzmann Law,  $\epsilon\sigma T^4$ . In terms of mass addition cooling, the fluid is added into the boundary layer resulting in a coolant barrier to the wall aerodynamic heating which has the effect of lowering the heat flux  $\dot{q}$ . Kattari<sup>(3)</sup> carried out experiments on spherical and blunt conical bodies to study the heat transfer effects from the mass addition. The mass can also be added in the form of film cooling as demonstrated by Zhang et al.<sup>(4)</sup> and Juhany et al.<sup>(5)</sup> whereby a thin film of fluid is injected near the stagnation point which then spreads around the body. Papas and Okuno<sup>(6)</sup> had investigated the effect on skin friction and heat transfer from gas injection at Mach number range  $0.7 \leq M \leq 4.35$  and Reynold number  $Re = 2.5 \times 10^6$ . In transpiration cooling, Glass et al.<sup>(7)</sup> simulated heat transfer cooling on the refractory composite material as used on engine combustor walls using a boundary layer method on a 2D configuration. Brune et al.<sup>(8)</sup> further investigated the effects of variable transpiration cooling in a 2D simulation to show that adjusting the injection velocity along the surface gave better results. Henline<sup>(9)</sup> too showed in a 2D axisymmetric simulation that the fluid is injected uniformly into the flow from a porous surface has led to heat transfer alleviation. Elsewhere ablation techniques as discussed by Chen and Henline<sup>(10)</sup> too have been used quite successfully to lower the heat flux to the vehicle surfaces. During the ablation process, the surface melts or decomposes and vapourises as it enters the boundary layer. The phase changing chemical reactions absorb significant energy from the freestream lowering of the heat transfer rates. The shape of the vehicle nose thus may change non-uniformly over time and can lead to pitching moment changes and other implications for aerodynamic and dynamic stability coefficients.

In the present work, the CFD method was first used to calibrate the ability of the numerical method to simulate hypersonic flows. Three well-known re-entry modules were selected from the literature and meshed appropriately for this investigation. The first of these models was the blunt conical forebody with a cylindrical shoulder almost replica of the Pioneer-Venus Galileo re-entry module as described in a paper by Mitcheltree et al.<sup>(11)</sup>. The second configuration examined in the present study was an Apollo model with dimensions as shown by Moss et al.<sup>(12)</sup>. Finally, an X-38 Space Shuttle configuration was obtained from open literature and a 3D CAD model was recovered from basic geometry. A 12-block mesh was produced using GRIDGEN and flow field simulations were produced to obtain heat fluxes and other pressure distributions which were then compared against the experiment from literature. A uniformly distributed outflow was then imposed as a boundary condition on the front blunt nose to examine heat alleviation effects due to transpiration cooling.

## 2.0 COMPUTATIONAL METHODOLOGY

It would be appropriate to provide some comments on the computational algorithm used for the present work. The conservative form of the compressible Reynolds-Averaged Navier-

Stokes equations in index form is given as follows:

$$\frac{\partial \rho}{\partial t} + \frac{\partial}{\partial x_i} [\rho u_i] = 0 \quad \dots(1)$$

$$\frac{\partial}{\partial t} (\rho u_i) + \frac{\partial}{\partial x_j} \left[ \rho u_i u_j + p \delta_{ij} - \left( 1 + \frac{\mu_t}{\mu} \right) \tau_{ij} \right] = 0 \quad \dots(2)$$

$$\frac{\partial}{\partial t} (\rho E) + \frac{\partial}{\partial x_j} \left[ \rho u_j E + u_j p - \left( 1 + \frac{\mu_t}{\mu} \right) u_i \tau_{ij} - \left( c_p \frac{\mu}{Pr} + c_p \frac{\mu_t}{Pr_t} \right) \frac{\partial T}{\partial x_j} \right] = 0 \quad \dots(3)$$

$\rho$  in these equations refers to the density,  $p$  the pressure and  $T$  is the temperature.  $E$  is the total energy and  $u$  is the velocity vector in tensor format.  $\tau_{ij}$  is the viscous stress tensor which may be written as

$$\tau_{ij} = \mu \left( \frac{\partial u_i}{\partial x_j} + \frac{\partial u_j}{\partial x_i} - \frac{2}{3} \frac{\partial u_k}{\partial x_k} \delta_{ij} \right) \quad \dots(4)$$

The Spalart–Almaras one-equation turbulence model is used to compute turbulent viscosity coefficient ( $\mu_t$ ) for most of the present computations. The Wilcox two equations  $k$ – $\omega$  model demanding increased computational time was tried in a few cases without noting any improvements in results. The Sutherland law is implemented to compute the laminar viscosity coefficient ( $\mu$ ). Since the flows computed involve hypersonic Mach number, the choice of the Prandtl number is selected to suite the Mach number whereas the use of specific heat and the specific heat ratio  $c_p/c_v$  ( $\gamma$ ) in the algorithm for one species gas must also respect the high Mach number flow conditions subject to the relations<sup>(13,14)</sup>:

$$c_v(T) = R \left( \frac{5}{2} + \frac{\left( \frac{h\nu}{kT} \right)^2 e^{-h\nu/kT}}{\left( e^{\frac{h\nu}{kT}} - 1 \right)^2} \right), \quad c_p(T) - c_v(T) = R$$

$$\frac{c_p(T)}{R} = \sum_{n=0}^{n=4} a_n T^n \quad \dots(5)$$

where  $T$  is the temperature,  $R$  is the real gas constant,  $h$  is Planck's constant,  $\nu$  is the fundamental vibrational frequency and  $k$  is Boltzman's constant and where  $a_n$  are curve-fit constants.

Above Navier–Stokes equations are the first cast into curvilinear co-ordinate scheme following the Vinokur transformation<sup>(15)</sup> method. The numerical algorithm used to solve the Navier–Stokes equations is an implicit factorization finite difference scheme which is described at length by Beam and Warming<sup>(16)</sup>. Local time linearisation is applied to the non-linear terms and, following Pulliam and Chausee<sup>(17)</sup>, an approximate factorisation scheme is applied to the resulting matrices which factorizes the operator itself resulting in efficient matrix equations with narrow bandwidth. This results in block tridiagonal matrices which are easy to solve. The spatial derivatives can thus be approximated using second-order central differences. Explicit and implicit artificial dissipation terms are added to achieve nonlinear stability. A spatially variable time step is used to accelerate convergence to steady-state solutions.

The input flow conditions ( $\rho$ ,  $\rho u_i$ ,  $e$ ) for the outflow surface must be evaluated from the jet mass, momentum and static pressure conditions at the exit boundary. If the jet mass flow rate ( $\rho u$ ) momentum ( $\rho u^2$ ) and jet static pressure ( $p_{out}$ ) are known, as indeed was the case in

Ref. 20, then  $\frac{p}{\rho_\infty}$  and  $\frac{\rho u}{\rho_\infty u_\infty}$  as well as the energy terms can be evaluated. These conditions are then treated like a new ‘slip’ condition which remains fixed during the flow-applied run. The algorithm iterates between the successive grid planes near the exit control boundary until the desired flow conditions are matched at the exit boundary as the convergence criterion is reached. For the corresponding solid surface run this surface would understandably carry a no-slip boundary. Alternatively, an outflow static pressure may be affixed at the control boundary to match the ultimate outflow conditions. The outflow pressure ( $p_{out}$ ) and the corresponding Mach number ( $M_{out}$ ) must be evaluated with respect to the pressure and the Mach number at the edge of the boundary layer. The boundary layer edge conditions may be obtained from a prior no outflow run. Other flow conditions for the algorithm may be evaluated as follows:

$$\begin{aligned} \frac{p_{out}}{p_e} &= \left[ \frac{1 + \frac{\gamma-1}{2} M_e^2}{1 + \frac{\gamma-1}{2} M_{out}^2} \right]^{\frac{\gamma}{\gamma-1}}, & u_{out} &= M_{out} \sqrt{\left\{ \frac{\gamma p_{out}}{\rho_{out}} \right\}} \\ e_{out} &= \frac{p_{out}}{\rho_{out}(\gamma-1)} + \frac{u_{out}^2}{2} \\ h e_{out} &= e_{out} + \frac{p_{out}}{\rho_{out}} \end{aligned} \quad \dots(6)$$

Heat transfer was also computed for the three models investigated in this paper. The heat transfer in a hypersonic flow field which consists of dissociated gases is given by the equation:

$$\dot{q}_w = k_{th} \left( \frac{\partial T}{\partial y} \right)_w + \left( \sum \rho D_i h_i \frac{\partial C_i}{\partial y} \right)_w \quad \dots(7)$$

where  $k_{th}$  is the thermal conductivity constant for the gas,  $h_i$  is the dissociation energy per unit mass of atomic products,  $D_i$  is the molecular diffusion constant of the  $i$ th-component of the mixture and  $C_i$  refers to the mass fraction. For the present analysis only, the first term in equation<sup>(7)</sup> was recovered directly from the computed flow field. The diffusion terms which can be significant at high temperatures and other radiative heat from excited atoms and molecules in the shock layer or even catalytic effects from chemical reactions are not addressed in this analysis. Following the experiment, the reference point heat transfer value  $\dot{q}_{wRef}$  was obtained from Fay–Riddell equation<sup>(18)</sup>:

$$\dot{q}_w = \frac{0.763}{(Pr_w)^{0.6}} \rho_e u_e^{0.4} \rho_w u_w^{0.1} [h_{oe} - h_w] \left[ 1 + (L_e^{0.52} - 1) \frac{h_d}{h_{oe}} \right] \left[ \left( \frac{du_e}{dx} \right)_t \right]^{0.5} \quad \dots(8)$$

w and e refer to the wall and boundary layer edge conditions,  $h_o$  is the total enthalpy condition and  $h_d$  is the dissociation enthalpy per unit mass of air in the external flow. The Prandtl number  $Pr_w$  value was 0.9 and the Lewis number  $L_e$  was assumed to be 1. The last term  $\left( \frac{du_e}{dx} \right)_t$ , in front of the blunt nose at the stagnation point  $t$  can be simply recovered from the relationship:

$$\left( \frac{du_e}{dx} \right)_t = \frac{1}{R} \sqrt{\frac{p_e - p_\infty}{\rho_\infty}} \quad \dots(9)$$

### 3.0 COMPUTATIONS

Navier–Stokes computations were performed on a number of hypersonic configurations. First validations were performed for the models used in actual wind tunnel experiments and, subsequently, more realistic hypersonic configurations were examined to see if the computations performed satisfactorily. The first of these is a cylindrical configuration supporting a hemispherical tip. The configuration shown in Fig. 1 was tested by Kaattari<sup>(19)</sup> at  $M = 7.32$  in the Reynolds number range  $0.6 \times 10^6$ – $5.2 \times 10^6$ . In the experiment, an externally supplied internal pressure of the model was balanced against the flow field external pressure to obtain the required mass flow rate through the porous frontal area. The mass flow rate profile was calculated in arbitrary units using a relationship of the form,  $\dot{m} = cA(P_{in}^2 - P_{ex}^2)$ , where  $c$  is a conductance constant at the point location,  $A$  is the sniffer tube area and  $P_{in}$  and  $P_{ex}$  refer to the chamber and external pressures. It is understood that the internal pressure is varied to obtain the non-constant velocity profile at the exit. The instrumentation is shown in Fig. 1. A complex flow profile was thus obtained at the leading edge. In the present computations, there were no means to vary the internal pressure against the external varying pressure field at the nose. A simplified constant exit velocity was applied to match a nominal mass flow rate of about  $\rho u / \rho_\infty u_\infty = 0.027$  used in the experiment. From this viewpoint, the exit outflow condition does not match exactly between simulation and the experiment.

The CFD-based simulation of the above experiment was carried out at  $M = 7.32$  and unit Reynolds number  $5.2 \times 10^6$ . The 3D mesh representing a  $15^\circ$  slice of the model used to simulate the flow is shown in Fig. 2. The Mach number-based flow field is also shown on the right-hand side of Fig. 2. The  $y^+$  value in all the models examined here was kept within a nominal value of 1. For more complex shapes discussed later, the  $y^+$  distribution around the surface is duly provided. A meticulous grid sensitivity study was carried out for each case discussed here. For brevity, these grid sensitivity results are not shown included here.

The computed pressure distribution for the solid surfaced model and the one supporting a flow ejection at the blunt hemispherical nose are shown in Fig. 3. The computed pressure agrees quite well with the measured pressure distribution. Note the low-pressure value at the stagnation region when the blowing is applied. Indeed owing to these low pressures at the stagnation region it would not be practical to apply the blowing across the entire region lest the aerodynamics performance is adversely affected. In the present case, therefore, the mass

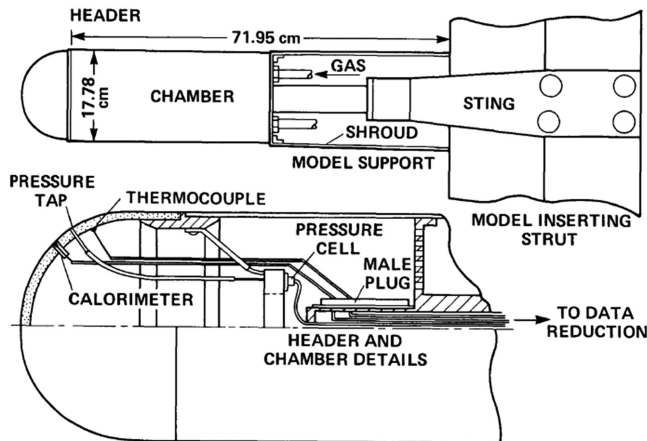


Figure 1. Model support and flow control mechanism, Kaattari<sup>(20)</sup>.

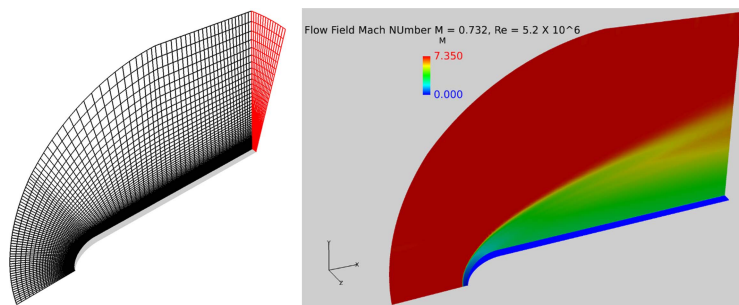


Figure 2. 3D mesh of a 15° sliced cylindrical model with a hemispherical nose,  $90 \times 100 \times 15$  (left). The computed Mach number field (right).

flow rate was applied to about 10% of the surface area adjacent to the stagnation region rather than the complete surface flow ejection profile used in the experiment.

Kaattari<sup>(19)</sup> explicitly states that the heat transfer performance of the model would be profoundly affected by the presence of the transition regime on the model surface, without actually defining the location or the extent of the transition region. The present computations were performed assuming fully turbulent flow without accounting for the transition effects. It should also be stated that the present method relies on holding the flow rates on the surface constant near the stagnation region rather than controlling the exact profile of the flow rates as depicted in the experiment. In a numerical simulation, it would be quite impractical to manually match the precise blowing coefficient from the experimental mass flow rate blowing profile at each grid point as an input boundary condition. Using a constant jet outflow instead of the varying mass flow rate depicted in the experiment would lead to some discrepancies. The comparison of the results from the present computations can thus only be considered as qualitative.

Figure 4 shows a comparison of the present results against the measurements from Kaattari<sup>(19)</sup>. As mentioned earlier, the computation was carried out for fully turbulent flows. No effects from transition mentioned in the experiment have been included. For the blowing simulation, no attempt has been made to simulate the ejection profile used in the experiment. It should also be noted that the increase in heating rate reduction in the experiment is consistent with the surface injectant flux profile that increases 50% from the stagnation point reaching a maximum near the heat flux minima. For the solid surface case, the computed heat transfer rates, while remaining fairly close to the experiment for the nose region tend to overpredict the heat flux towards the straight portion. The concentrated flow ejection in the close vicinity of the stagnation region leads to substantially lower values of heat transfer rates adjacent to the nose as opposed to the experimental results showing a maximum heat transfer rate at the apex followed by notable cooling, almost reaching the computed values at about 2.5 cm from the nose. The computed results show a maximum heat transfer at  $S \approx 3.5$  cm, whereas the experiments show a second peak at  $S \approx 6.5$  cm. Both computed and the experimental results for the flow ejection case remain very close beyond  $S \approx 6.0$  cm, but always below heat transfer rate values for the solid surface case.

Figures 5 and 6 show the velocity vectors at the blunt surface near the stagnation region. Not only does the injectant flow cause a barrier between the surface and the free stream but also redirects the flow upstream of the body as the flow is decelerated. Note the change in the shape of the velocity profiles at the surface from blowing.

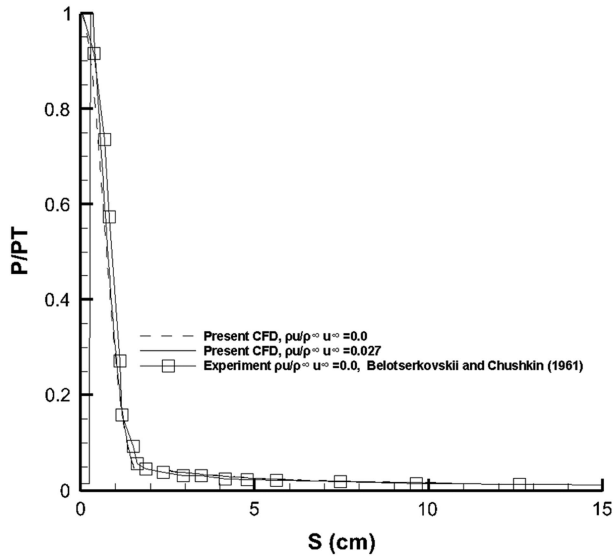


Figure 3. Pressure distribution comparison for the hemispherically tipped cylindrical model.

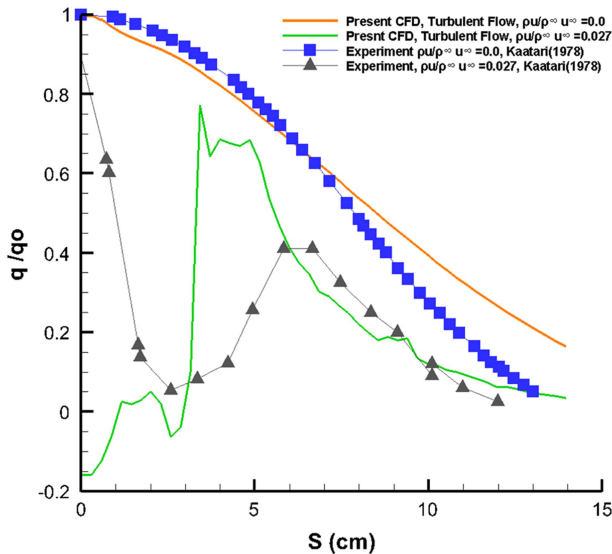


Figure 4. Heat transfer comparison with experiment,  $M=7.32$ ,  $Re_D=1.1 \times 10^6$ .

A round blunt-nosed cone ogive and a sharp blunt-nosed ogive cone were selected from the experiments carried out by Nowak<sup>(20)</sup> as further two wind tunnel models to validate the present computational method. The computed Mach number flow field is shown in Fig. 7.

It is clear that the flow ejection has the effect of pushing the shock wave away from the nose. The flow field in the vicinity of the blunt nose is radically changed owing to blowing with large areas of decelerated flow responsible for heat reduction. There is a larger region of decelerated flow between the shock and the blunt round nosed cone when ejection is applied. Note also the presence of the jet shock near the nose of the round nose airfoil. The



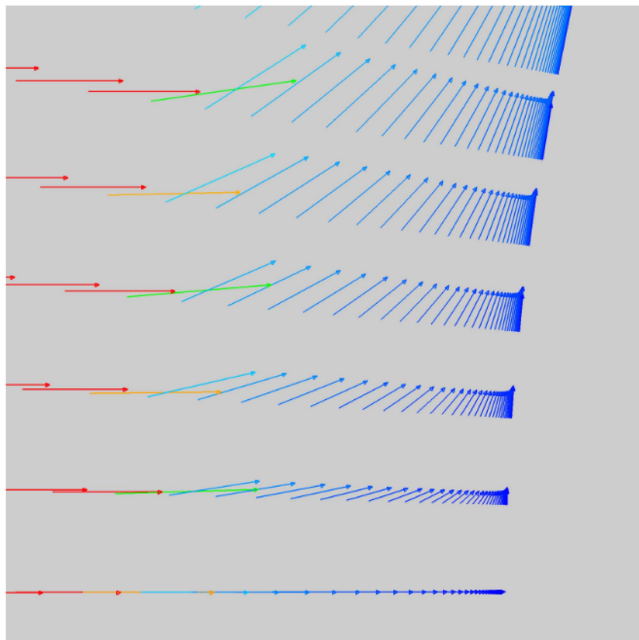


Figure 5. Velocity vectors (solid surface).

momentum vectors superimposed upon the Mach number flow field for the sharp-nosed cone are shown in Fig. 7 (c) and (d) that there is the presence of strong recirculation and reversal of the flow near the sharp corner of the cone with a clear reattachment point downstream of the corner. The detailed flow field can also be compared with the shadowgraphs in Fig. 8, taken from Nowak<sup>(20)</sup>. The solid nosed cone results match up closely with the experiment whereas the sharp-nosed results with blowing ( $\rho u/\rho\infty u\infty = 4.68$ ) show a complex flow pattern in front of the nose. The distinct round contour next to the shock is the jet mainstream interface present in both computations and the shadowgraph. The jet normal shock too is visible in both pictures.

The pressure distribution comparison for the two models against the available experimental data is shown in Fig. 9. For the round nosed ogive cone, only the solid surface results were available, whereas for the sharp nose, ogive cone only the flow applied data was available.

The round nosed computed results shown by the solid curve remain fairly close to the experimental data depicted by square symbols. The flow is understandably transformed near the nose by blowing but follows the solid body results away from the nose. The sharp-nosed solid surface results are somewhat higher than the corresponding round nosed cone results on most of the surface. The blowing on sharp-nosed results are different at the nose region, and are again a little higher than the corresponding experimental results represented by the filled squares.

The results from the heat transfer computations are shown in Fig. 10. The computed results on the solid body round nosed cone are represented by the solid line curve and they show an increasing heat transfer rate trend near the nose as indeed does the experimental data. The results on the surface away from the nose too are well matched. However, the computations do not resolve the notable depression in heat transfer rates just past the nose region. The flow ejection results indicated by the dashed curve show a notable decrease in heat transfer results near the nose before settling down to a value of  $q/q_o = 0.05$  away from the nose. The solid

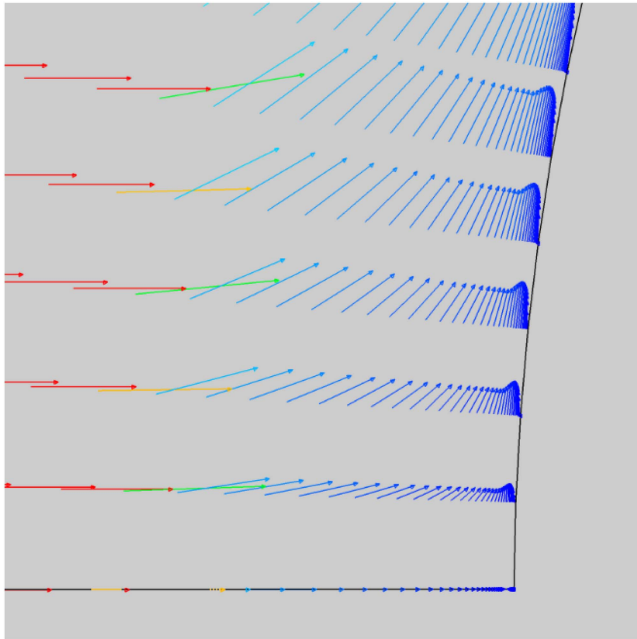


Figure 6. Velocity vectors flow ejection case  $\rho u/\rho_\infty u_\infty = 0.027$ .

sharp-nosed cone consistently shows higher heat transfer rate than the solid round cone. The flow ejection results show lower values than the corresponding solid body results up to  $S/L = 0.5$  beyond which they show an increasing trend. The heat transfer experimental data for the flow ejection data for the sharp-nosed cone shows a decreasing trend near the nose which is the same as the computed results.

The next series of models examined the hypersonic flow past configurations which have been used in real-life projects. The first of these is the Venus–Galileo model shown in Fig. 11. It consisted of a blunt cone fore body of bluntness  $R_N/R_B = 0.5$  with a base diameter of 1 m and a conical surface of  $45^\circ$  half-angle which abuts smoothly on to a cylindrical shoulder which has a radius of 0.1 m. The dimensions of the forebody corresponded to the Pioneer–Venus–Galileo rocket as provided by Micheltree<sup>(11)</sup>. Figure 12 shows the single block of a mesh of dimensions  $83 \times 127 \times 45$  used for this simple forebody. The  $y+$  value for the first grid line in the normal direction to the solid wall was kept in between 1 and 2 along the axial length of the model.

The pressure distribution at  $M_\infty = 10$ ,  $\alpha = 0^\circ$  and  $R = 10 \times 10^6$  at the spherical blunt nose is shown in Fig. 13. In order to avoid sonic choking conditions at the outflow boundary, only a small mass flow  $\frac{\rho u}{\rho_\infty u_\infty} = 0.01$  was tested for the blowing case in the nose region.

It can be seen that a very strong shock immediately upstream of the nose at a very small standoff distance which is very consistent with the flow at  $M = 10$ . The blowing has a profound effect upon the pressure field in the vicinity of the nose and the introduction of the additional mass flow from the outflow boundary at a relatively higher static pressure dilutes the high stagnation region between the nose and the shock. A comparison of the computed pressure distribution against the experimental data extrapolated for a  $45^\circ$  blunt cone from Belotserkovskii and Chushkin<sup>(21)</sup> is given in Fig. 14.

The agreement between the computed and the extrapolated data from Belotserkovskii and Chushkin<sup>(21)</sup> is quite satisfactory. The pressure distribution calculations for the leading edge blowing

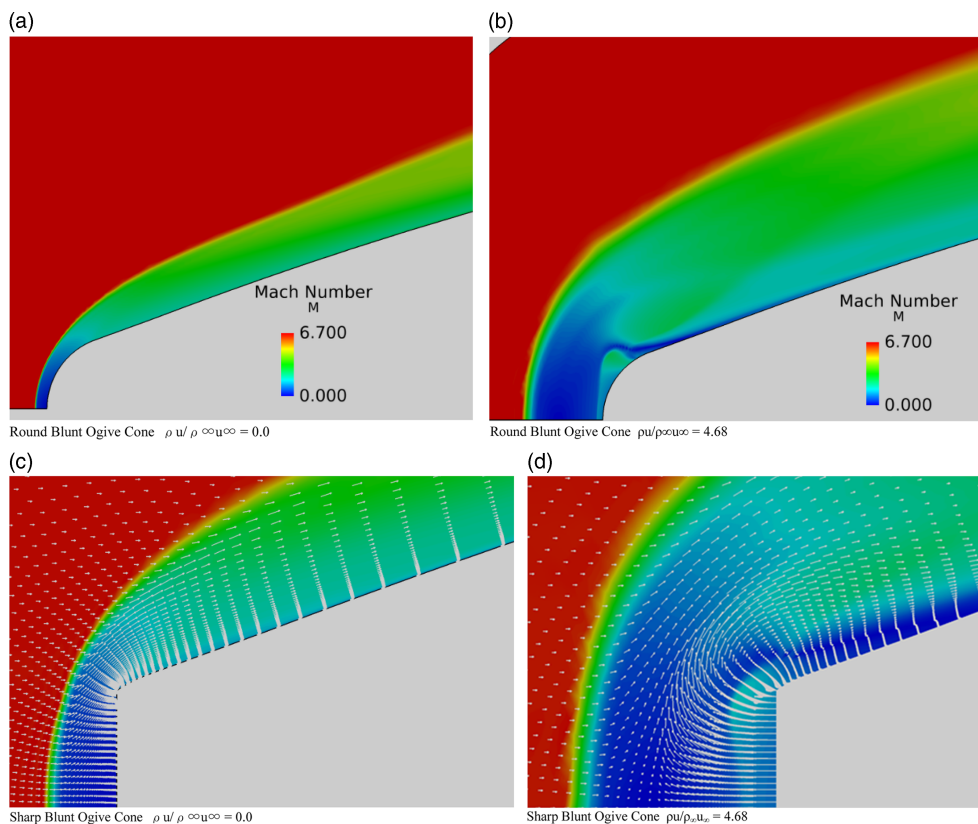


Figure 7. Mach number flow field,  $M = 6.8$ ,  $Re = 1.3 \times 10^6$ ,  $\alpha = 0.0^\circ$ . (a) Round blunt ogive cone  $\rho u / \rho_\infty u_\infty = 0.0$ . (b) Round blunt ogive cone  $\rho u / \rho_\infty u_\infty = 4.68$ . (c) Sharp blunt ogive cone  $\rho u / \rho_\infty u_\infty = 0.0$ . (d) Sharp blunt ogive cone  $\rho u / \rho_\infty u_\infty = 4.68$ .

case follow the solid surface case quite closely and are not repeated here. The heat flux calculations were also carried out for this Galileo configuration. The heat flux values normalized with respect to the stagnation point using the Fay–Raydell technique mentioned above are shown in Fig. 15.

Across the blunt nose region itself where the cooler air is just entering the flow field, the heat transfer rate as in the previous cylindrical nose model, is noticeably lower than the solid boundary case. The lower heat transfer rates established for the blowing case at the nose are carried through to the conical region until the shoulder location where the two results from the ejection case and solid boundary case equalize. The velocity contours near the blunt surface of the model for the solid surface and the blowing surface are shown in Figs 16 and 17. Note how the first contour for the blowing case indicates a reversed blowing flow at the blunt surface in place of the no-slip condition for the solid surface case.

Figures 18 and 19 show the shock location in the Mach number flow field distribution near the blunt nose of the two cases under study. For the solid surface case in Fig. 14, the centre of the shock location identified as the red-yellow boundary is seen to be at grid point about 5.3 counting from the left. For the outflow case in Fig. 15, the red-yellow boundary appears to be relatively closer to grid point 5 from the left. The small outflow ( $\rho u / \rho_\infty u_\infty = 0.01$ ) has the effect of pushing the shock slightly away from the blunt nose.

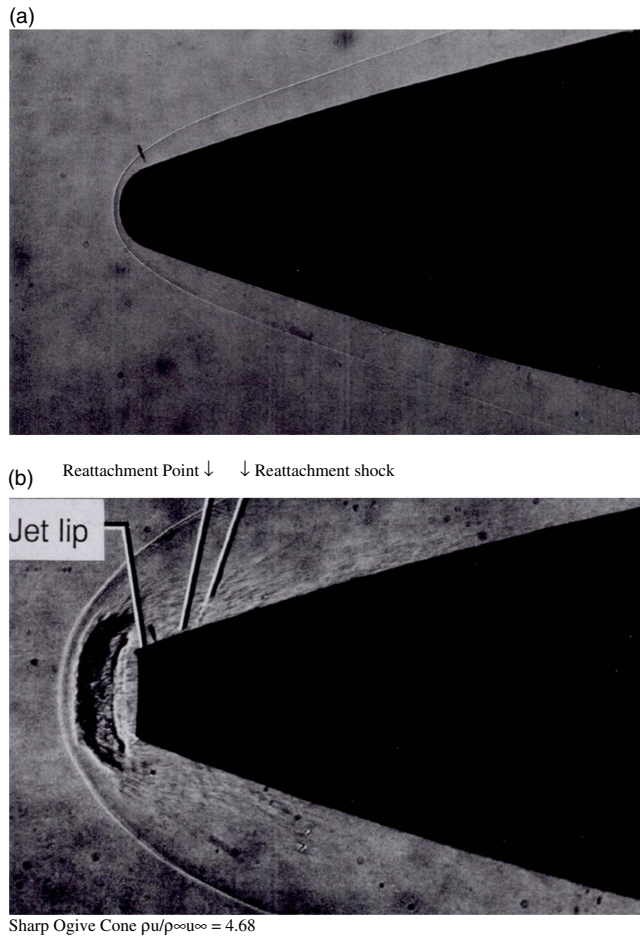


Figure 8. Shadowgraphs of round nosed and sharp nose ogive cones in hypersonic flow, Nowak (1988).  
 (a) Round Blunt Ogive Cone  $\rho u/\rho_{\infty} u_{\infty} = 0.0$ . (b) Sharp Ogive Cone  $\rho u/\rho_{\infty} u_{\infty} = 4.68$

The grid for the Apollo configuration (Fig. 20) as used in the present study is shown in Fig. 21. The 2D grid shown on the right-hand side was rotated through  $90^\circ$  to produce the 3D configuration. The basic dimensions for the grid were obtained from Moss et al.<sup>(12)</sup>. The  $y^+$  dimension on the surface remained less than 1 everywhere on the surface of the configuration.

The CFD computation was carried out once again at  $M = 10$ ,  $Re = 1.1 \times 10^6$  and  $\alpha = 0$  Deg. Figure 22 shows the pressure coefficient distribution on the model and the flow field.

The pressure distribution obtained from the present solid surface case was compared against the measurement as reported by Bertin<sup>(22)</sup> in Fig. 23.

The agreement between the computed measured values and the experiment is very good for the front spherical surface. The back conical surface as shown in Fig. 24 suffers from large-scale flow separation at the trailing of the model which may not be well resolved by the current one-equation Spalart–Allmaras turbulence model. Even then the comparison of pressures as observed in Fig. 24 is quite good. The heat flux was also computed on the back surface of the configuration (Figs 25). A reversing separated flow would give rise to increasing heat transfer rates towards this region. A comparison of results for the front blunt surface against the experimental data is shown in Fig. 26. The flow ejection case shows heat

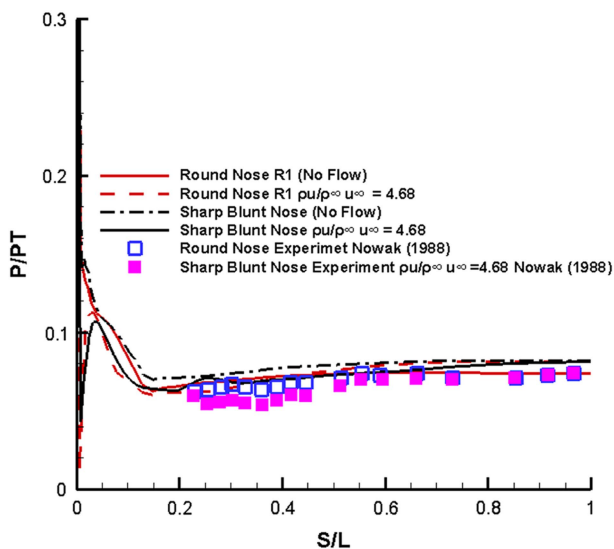


Figure 9. Normalized pressure distribution  $M = 6.8$ ,  $Re = 1.3 \times 10^6$ ,  $\alpha = 0.0^\circ$ .

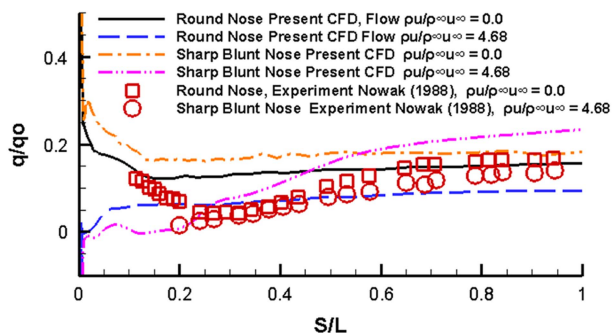


Figure 10. Heat transfer results  $M = 6.8$ ,  $Re = 1.3 \times 10^6$ ,  $\alpha = 0.0^\circ$ .

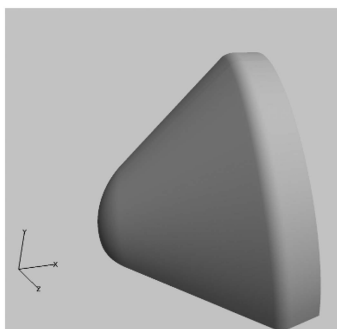


Figure 11. Pioneer–Venus–Galileo model.

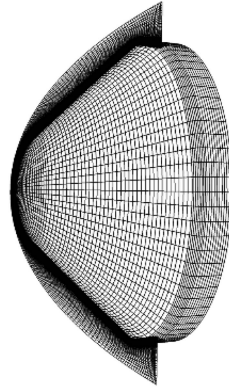


Figure 12.  $83 \times 127 \times 45$  mesh.

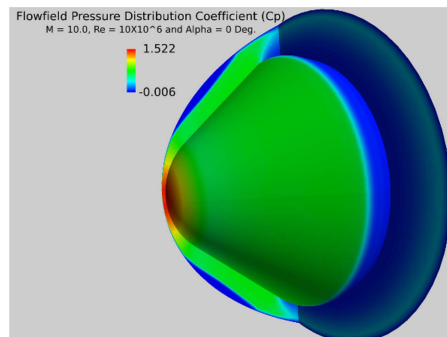


Figure 13.  $C_p$  distribution solid surface.

transfer values lower than those for the solid surface. Within the error margin of the experiment, the computed results matched well with the measurements.

A comparison of the results between the flow injection case and the solid surface case for the back conical surface is shown in Fig. 27. It is clear that the heat transfer rate at the back conical portion is a small fraction of the heat transfer rate at the blunt region. The figure shows that the distances greater than 0.5 with injection reduces the heat transfer in the base of the body. This could possibly be due to the fact that the injectant defies the mixing imposed by the highly turbulent wake, or perhaps as indicated in Fig. 25, it acts as a barrier attached to the base.

Finally, CFD-based simulations were carried out to study the flow field past the X-38 Space Shuttle. The dimensions were taken directly from the published 3-view data (Fig. 28) from the literature<sup>(23)</sup>. A cad model of the orbiter was produced from this figure. Since the details in the inner portions (especially the valleys in between the wing and the body) were only extrapolated from a blown up version of the simple drawing, it is difficult to say if the final model was as accurate. The various protuberance on the top surface were ignored to produce a simple model convenient for CFD simulations. The 3-view drawing used to reproduce the cad model is shown in Fig. 28 along with the 3D model displaying the surface grid which consisted of 12 blocks comprising some 175,000 grid points in Fig. 29.

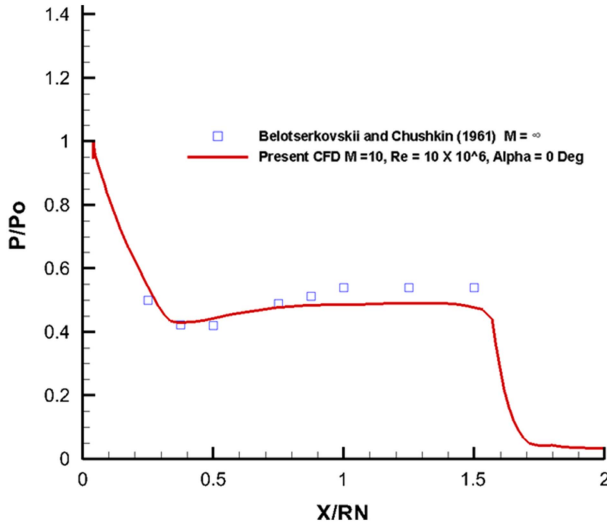


Figure 14. Pressure distribution on the blunt fore body,  $M = 10, Re = 10 \times 10^6, \alpha = 0^\circ$ .

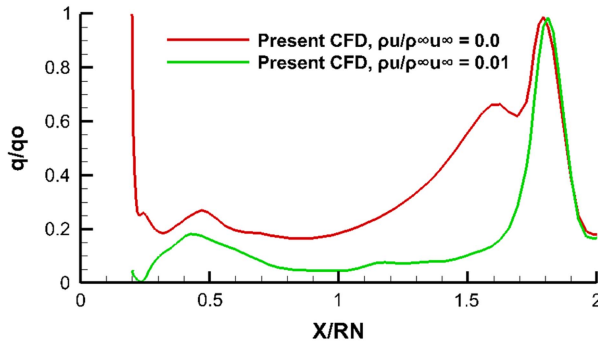


Figure 15. Heat flux on the blunt fore body,  $M = 10, Re = 10 \times 10^6, \alpha = 0^\circ$ .

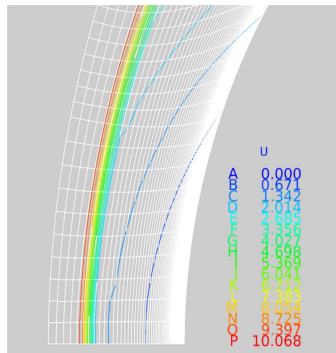


Figure 16. Velocity contours (solid surface).

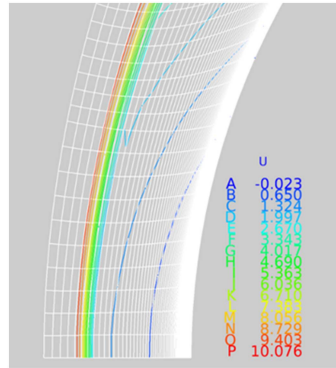


Figure 17. Velocity contours flow ejection case  $\rho u/\rho_\infty u_\infty = 0.01$ .

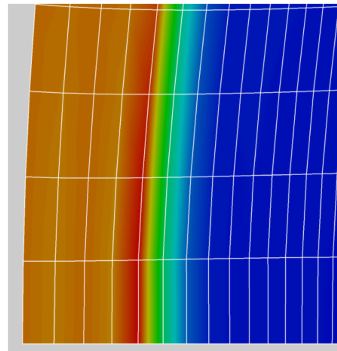


Figure 18. Shock location (solid surface).

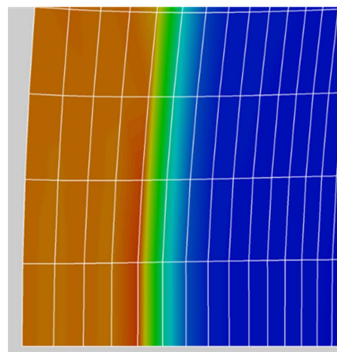


Figure 19 . Shock location, flow ejection case  $\rho u/\rho_\infty u_\infty = 0.01$ .

The  $y^+$  values on the major blocks encapsulating the main geometry surfaces are shown in Fig. 30. Every effort was made to keep on  $y^+$  value close to below 1 for the bottom surface where most of the heat transfer occurs.



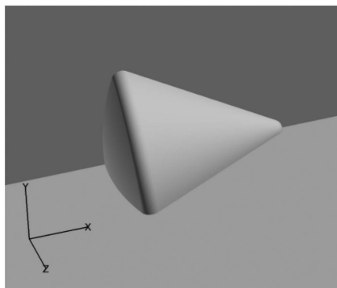


Figure 20. Apollo configuration.

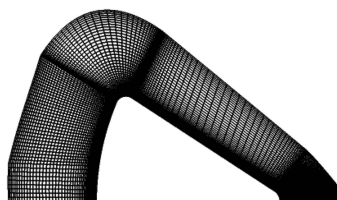


Figure 21. 2D grid ( $100 \times 121$ ).

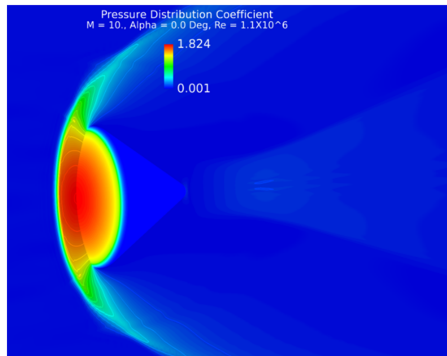


Figure 22.  $C_p$  distribution solid surface  $M = 10$ ,  $Re = 1.1 \times 10^6$ ,  $\alpha = 0^\circ$ .

The flow field pressure distribution obtained on the X-38 surface is shown in Fig. 31. Figure on the left-hand side shows the pressure distribution on the complete model. The figure on the right includes the pressure field on a reflection plane running through the centre of the model.

It is noted that region of high pressure exists near the nose of the model with the stagnation point well below the nose. The flow field across the reflection plane confirms that most of the flow activity is concentrated on the lower pressure side with the pressures on the leeward side drop to low values immediately past the nose region. Figure 32 shows the pressure field where the exit pressure at the nose boundary was fixed to give an outflow  $M_{out} = 0.3$ . The exit pressure was calculated by considering the flow Mach number and pressure at the edge of the

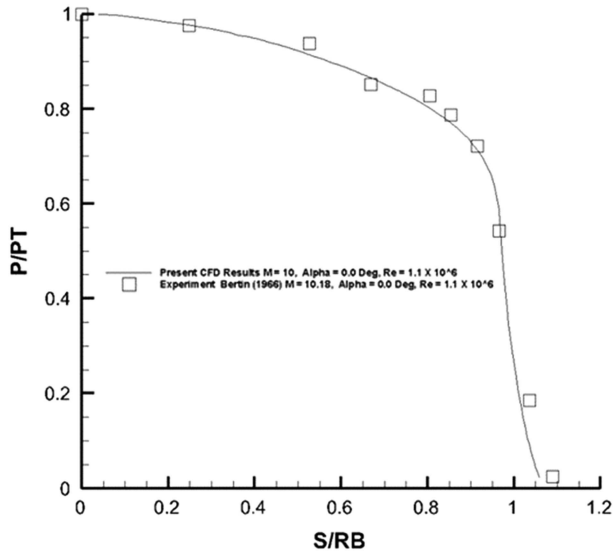


Figure 23. Pressure distribution on the front spherical portion of the Apollo configuration.

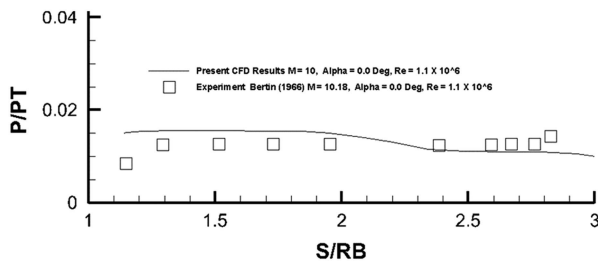


Figure 24. Pressure distribution on the back conical portion of the Apollo configuration.

boundary layer. The static pressure was then calculated to give a  $M_{\text{out}} = 0.3$  at the surface. The outflow from the solid boundary is immediately affected by the flow accelerating round the blunt nose and the resulting velocity field at the solid surface is shown on the right-hand side of Fig. 32. It is, of course, obvious that no such velocity vector field is available for the solid boundary case.

The computed pressure distribution at  $M=6$  and Reynolds numbers  $Re = 3.1 \times 10^6$  and  $8.1 \times 10^6$  were compared against measurements taken from Leduke and Krogmann<sup>(24)</sup>. For the lower Reynolds number  $Re = 3.1 \times 10^6$ , the computations were conducted for a laminar flow as indeed was done in Ref. 24. For the higher Reynolds number  $Re = 8.1 \times 10^6$ , Spalart–Allmaras one equation was used for the complete model. Transition fixing was not attempted as the present solver as yet is not equipped with the capability. The comparison for both flows is shown in Figs 33 and 34.

It appears that for this laminar flow case in Fig. 35, for the outboard station cut, the comparison with experiment is quite good. In the region between  $0.8 < X/L_{\text{ref}} < 0.84$ , the flow is separated and reversing. Still, the agreement between computed results and measurements is good. The disconnect in the pressure curve at  $X/L_{\text{ref}} \sim 0.815$  is due to the

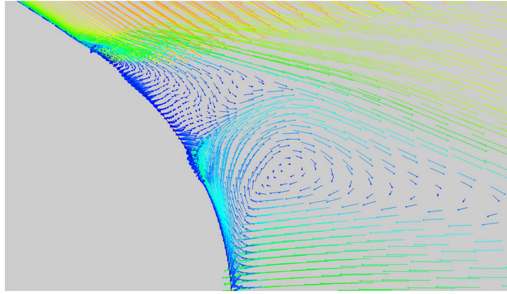


Figure 25. Separated and reversing flow at the trailing end of the Apollo model.

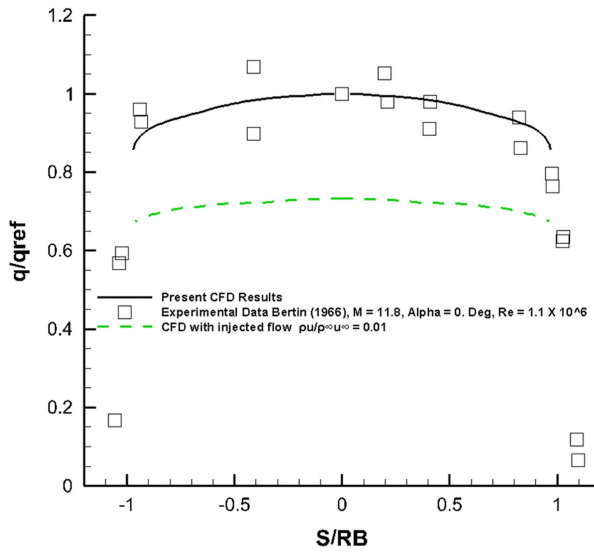


Figure 26. Heat flux on the blunt face,  $M = 10$ ,  $Re = 1.1 \times 10^6$ ,  $\alpha = 0^\circ$ .

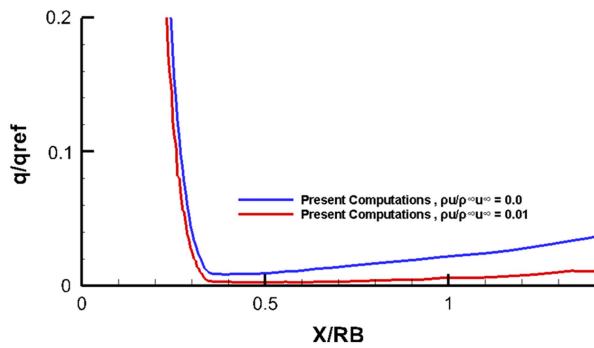


Figure 27. Heat flux in the axial direction,  $M = 10$ ,  $Re = 1.1 \times 10^6$ ,  $\alpha = 0^\circ$ .

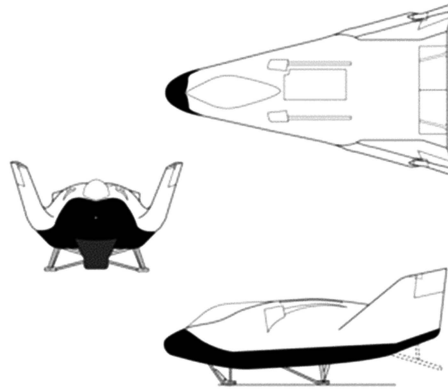


Figure 28. Length: 30 ft 0 in (36 ft including deorbit propulsion system rocket).

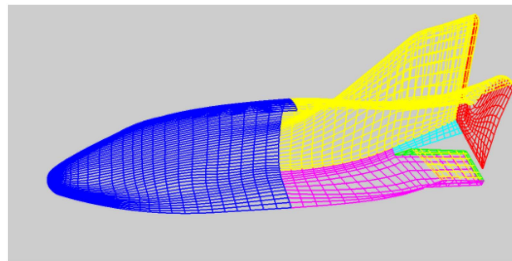


Figure 29. A simple X-38 CAD model showing the surface mesh.

fact that almost two coincident points lie on two adjacent blocks where the first point is on the main body and the second point is on the flaps deflected at  $20^\circ$ . Figure 34 shows the same comparison case for a turbulent flow at  $Re = 8.1 \times 10^6$ . Once again the one equation Spalart–Allmaras turbulence model has done reasonably well in being able to resolve this turbulent flow. Since the cad model was produced from dimensions extrapolated from a 3-view technical it is quite possible that there were some small differences between the current model and the exact geometry used in the experiment. The comparisons, however, are very encouraging. The heat flux results with and without the boundary outflow are shown in Figs 35 and 36. The stagnation point value of the heat flux ( $q_{ref}$ ) was used to normalize the results. It must, of course, be mentioned that the present method does not account for any diffusion, flow dissociation or other radiative effects.

For the laminar flow case in Fig. 35, the computations follow the general experimental trends quite faithfully. Only in the flow separation region just before the flaps, it is unable to resolve the higher level of heat activity. The outflow case depicted by the dashed lines indicate that even with this high angle-of-attack ( $\alpha = 40^\circ$ ), where the tendency for the injected out flow is to move towards the leeward side, the blowing does appear to alleviate the heat flux. For the turbulent case in Fig. 36, there is an encouraging attempt by this one-equation model to come fairly close to the experimental values. The blowing off course has not performed as well as the earlier laminar case.

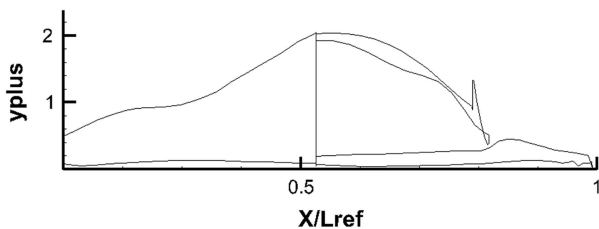


Figure 30.  $y^+$  distribution across the surface of the X-3D Space Shuttle Orbiter.

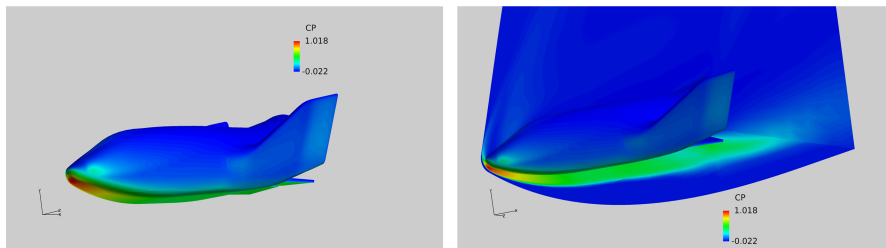


Figure 31.  $C_p$  distribution solid surface,  $M=8$ ,  $Re=8.1 \times 10^6$ ,  $\alpha=40^\circ$ .

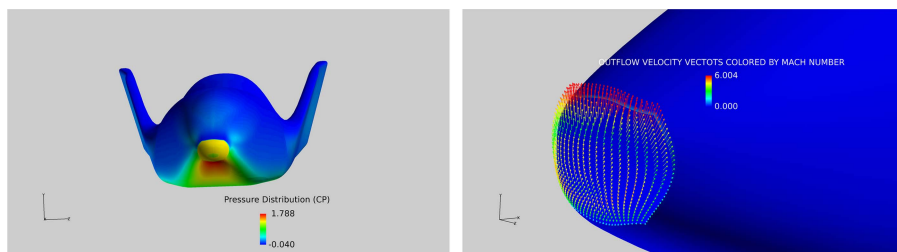


Figure 32.  $C_p$  distribution (left) and the velocity vectors (right) with flow injection at the leading edge,  $M=8$ ,  $Re=8.1 \times 10^6$ ,  $\alpha=40^\circ$ ,  $M_{out}=0.3$ .

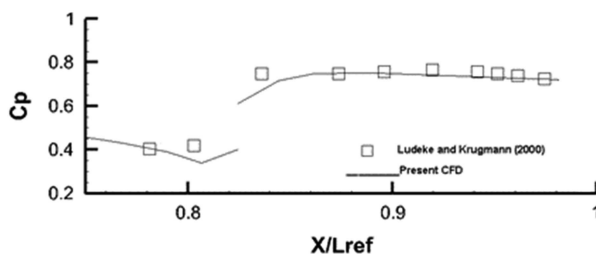


Figure 33.  $C_p$  distribution  $M=6$ ,  $Re=3.1 \times 10^6$ ,  $\alpha=40^\circ$ , laminar flow.

### 4.0 CONCLUSION

The CFD method has performed quite well in being able to resolve the flow for re-entry type vehicles in hypersonic Mach number regime.

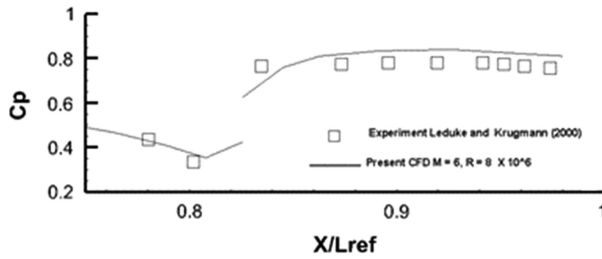


Figure 34.  $C_p$  distribution  $M=6$ ,  $Re=8.1 \times 10^6$ ,  $\alpha=40^\circ$ , turbulent flow.

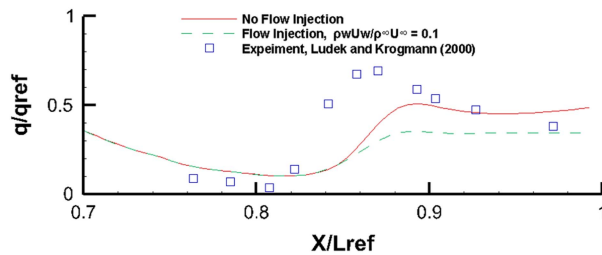


Figure 35. Heat flux,  $M=6$ ,  $Re=3.1 \times 10^6$ ,  $\alpha=40^\circ$ , laminar flow.

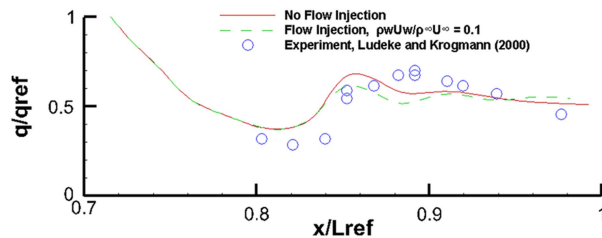


Figure 36. Heat flux,  $M=6$ ,  $Re=8.1 \times 10^6$ ,  $\alpha=40^\circ$ , turbulent flow.

It was found that spherical nose blunting provides better heat alleviation than the sharp-edged nose bluntness. The leading edge blowing appears to alleviate heating by thickening the boundary layer along the surface. The heat alleviation effects owing to frontal blowing were most noticeable near the blunt nose. The blowing also pushes the strong shock away from the blunt nose. In the regions supporting large regions of separated or reversing flow, the benefits from a thickened boundary layer may not be as straight forward. Unless the outflow conditions are determined to replicate the experimental blowing, disagreement between measurement and simulation as indeed observed in the first spherical nose cylindrical configuration will persist. The agreement between the experiment and computational conditions is all the more important when accounting for the transition effects in heat transfer predictions. The present computations were generally carried out for fully turbulent flows and heating effects owing to the presence of transition were ignored which must be responsible for some anomalies in the computed results.

Some further experimental data on a simple body under controlled flow conditions with known transition locations would go a long way in confirming the validity of the method.

The present engineering approach and the experimental data presented in this study demonstrate that its success is very much in developmental stages, with an intent to further investigate different blowing strategies and a comprehensive validation against experiment.

## ACKNOWLEDGEMENTS

This work was funded by the Deanship of Scientific Research, King Abdul Aziz University, Jeddah, under the Grant no. 135-112-D1438. The authors, therefore, acknowledge with thanks DSR for their technical and financial support.

## REFERENCES

1. HANKEY, W.L. *Re-Entry Aerodynamics*, 1988, AIAA Education Series, American Institute of Aeronautics and Astronautics, Washington, DC, USA.
2. STUMPF, D. K. *Titan II – A History of Cold War Program*, University of Arkansas Press, Fayetteville, USA, 2000.
3. KATTARI, G. E. Effects of Mass Addition on Blunt-Body Boundary-Layer Transition and Heat Transfer, NASA Technical Paper 1139, Ames Research Center, Moffett Field, California, 1978.
4. ZHANG, M., XIANG, S. and TONG, J. Film Cooling Effectiveness for Hypersonic Vehicles, The 22<sup>nd</sup> International Conference on Sound and Vibration, 12-16 July 2015, Florence, Italy.
5. JUHANY, A. K., HUNT, M. L. and SIVO, J. M. Influence of Injectant Mach Number and Temperature on Supersonic Film Cooling, *J of Thermophysics and Heat Transfer*, Jan-March, 1994, **8**, (1), 59–67.
6. PAPPAS, C. C. and OKUNO, A. F. The Relation between Skin Friction and Heat Transfer for the Compressible Turbulent Boundary Layer with Gas Injection, NASA TN D 2857.
7. GLASS, D. E., DILLEY, A. D. and KELLY, H. N. Numerical Analysis of Convection/Transpiration Cooling, NASA/TM-1999-209828, NASA, Hampton, Virginia, December 1999.
8. BRUNE, A., HOSDER, S., GULLI, S. and MADDALENA, L. Variable transpiration cooling effectiveness in laminar and turbulent flows for hypersonic vehicles, *AIAA J*, January 2015, **53**, (1), 176–189.
9. HENLINE, W. D. Transpiration Cooling of Hypersonic Blunt Bodies with Finite Rate Surface Reactions, NASA Contractor Report 177516, February 1989, NASA. Ames research Center, Moffat Field, California, USA.
10. CHEN, Y.-K. and HENLINE, W. D. Hypersonic non-equilibrium Navier–Stokes solutions over an ablating graphite nose tip, *J of Spacecraft and Rockets*, 1994, **31**, (5), 728–734.
11. MITCHELTREE, R. A., MOSS, J. N., CHEATWOOD, F. M., GREENE, F. A. and BRAUNQ, R. D. Aerodynamics of the Mars Microprobe Entry Vehicles, AIAA Paper 97-3658, 1997.
12. MOSS, J. N., GLASS, C. E. and GREENE, F. A. DSMC Simulations of Apollo Capsule Aerodynamics for Hypersonic Rarefied Conditions, 9th AIAA/ASM Thermophysics and Heat Transfer Conference, 5–8 June, San Francisco, USA.
13. GRUNDMANN, R. *Aerothermodynamik*, Springer Verlag, Berlin, Germany, 1st ed, Technische Universität Dresden, 2000.
14. GORDON, S. and MCBRIDE, B. J. Computer program for calculation of complex chemical equilibrium compositions and applications. Technical report, National Aeronautics and Space Administration, Office of Management, Sciatic and Technical Information Program, 1994.
15. VINOKUR, M. Conservation equations of gas dynamics in curvilinear coordinate system, *J of Computational Physics*, 1974, **14**, (2), pp 105–125.
16. BEAM, R. and WARMING, R. F. An implicit finite difference algorithm for hyperbolic systems in conservation law form, *J of Computational Physics*, September 1976, **22**, (1), pp 87–110.

17. PULLIAM, T. and CHAUSSEE, D. S. A diagonal form of an implicit approximate-factorization algorithm, *J of Computational Physics*, March 1981, **39**, (2), pp 347–363.
18. FAY, J. A. and RIDDELL, F. R. Theory of Stagnation Point Heat Transfer in Dissociated Air, *J of the Aeronautical Sciences*, Feb. 1958, **25**, (2), pp 73–85, 121.
19. KAAATARI, G. E. Effects of Mass Addition on Blunt-Body Boundary-Layer Transition and Heat Transfer, NASA Technical Paper 1139, 1978
20. NOWAK, R. J. Gas-jet and Tangent Jet-slot Film Cooling Tests of a 12.5° cone at Mach Number 6.7, NASA Technical Paper 2786, May 1988.
21. BELOTSERKOVSKIL., O. M. and CHUSHKIN, M. I. [1961] Hypersonic flow past Blunt Cones. Fluid Dynamics Symposium, Jablona, September 1961.
22. BERTIN, J. *The effect of Protuberances, Cavities, and Angle of Attack on the Wind Tunnel Pressure and Heat Transfer Distribution for the Apollo Command Module*, NASA TM X 1243, Manned Space Craft Center, Houston, Texas, 1966.
23. [https://en.wikipedia.org/wiki/NASA\\_X-38](https://en.wikipedia.org/wiki/NASA_X-38)
24. LUDEKE, H. and KROGMANN, P. Numerical and Experimental Investigation of Laminar and Turbulent Boundary Layer Transition, European Congress on Computational Methods in Applied Sciences and Engineering, 11–14 September 2000, ECCOMAS 2000.